

# On-demand phototoxicity inhibition of sensitizers and H<sub>2</sub>S-triggered *in-situ* activation for precise therapy of colon cancer



Mei Wen <sup>a</sup>, Nuo Yu <sup>a</sup>, Zhigao Yi <sup>b</sup>, Pu Qiu <sup>a</sup>, Cheng Tao <sup>a</sup>, Daniel K. Macharia <sup>a</sup>, Meifang Zhu <sup>a</sup>, Zhigang Chen <sup>a,\*</sup>, Xiaogang Liu <sup>b,c,\*</sup>

<sup>a</sup> State Key Laboratory for Modification of Chemical Fibers and Polymer Materials, College of Materials Science and Engineering, Donghua University, Shanghai 201620, China

<sup>b</sup> Department of Chemistry, National University of Singapore, 3 Science Drive 3, Singapore 117543, Singapore

<sup>c</sup> The N1 Institute for Health, National University of Singapore, Singapore 117456 Singapore

## ARTICLE INFO

### Article history:

Received 11 January 2023

Received in revised form 28 March 2023

Accepted 24 April 2023

Available online 1 May 2023

### Keywords:

Nanoframework, photosensitizer

Phototoxicity

Reactive oxygen species

Cancer therapy

## ABSTRACT

Conventional photo/sonosensitizers act on foci and normal tissues with limited selectivity, leading to severe skin and retina phototoxicity. Here we present a copper-hematoporphyrin monomethyl ether nanoframework (CuHF) that suppresses fluorescence on healthy tissues without generating reactive oxygen species, thus preventing phototoxicity to the skin and eyes. This nanoframework can react with endogenous hydrogen sulfide in colon cancer cells to generate CuS nanoparticles and Cu-HMME complexes *in situ*, enabling simultaneous photothermal and sonodynamic therapies. By leveraging strengths from coordination chemistry, material synthesis, and photochemistry, our study provides insight into the rational design of prodrug-like photosensitizers for high-precision targeted cancer therapy.

© 2023 Elsevier Ltd. All rights reserved.

## Introduction

There is a growing consensus that reactive oxygen species (ROS)-induced therapies including photodynamic therapy (PDT) and sonodynamic therapy (SDT) are the strategies of choice for tumor treatment due to the safety and noninvasive features of both light and ultrasound [1,2]. Various ways of sensitization have been proposed, among which the involved prominent materials include inorganic sensitizers (Titanium dioxide (TiO<sub>2</sub>) [3] and noble metal [4]), organic sensitizers (protoporphyrin [5] and hematoporphyrin monomethyl ether (HMME) [6]), and metal-organic frameworks (MOFs) [7,8]. Previous studies have mainly focused on making sensitizers excitable at long wavelengths and low power by manipulating the photon harvesting, the efficiency of intersystem crossing, and the retention of the triplet state [9–12]. For example, HMME as a second-generation porphyrin-related photosensitizer can be triggered by 630 nm light at 2.8 J/cm<sup>2</sup> [10], while BODIPY derivatives are excited by 630 nm light under 6 J/cm<sup>2</sup> [11,12]. Considerable efforts have succeeded in significant improving the photoactivation ability

of sensitizers, but this raises serious concerns about phototoxicity because they are also functionally activatable in normal tissues [1,13]. Patients administrated sensitizers are suggested to wear sunglasses, a hat and long-sleeved clothing for several weeks to prevent from prolonged photosensitivity. Thus, the development of a clinical application of sensitizers remains a formidable challenge because of the side-effects emanating from the undesired phototoxicity.

To alleviate the phototoxicity, the manipulation of the photoactivity of sensitizers has been proposed as an attractive method that relies on an “OFF-ON” two-step route. The first step is to turn off the photoactivity of sensitizers (A<sub>on</sub>→B<sub>off</sub>) through aggregation-caused quenching (ACQ) (such as Cu-TCPP [14], fucoidan-based theranostic nanogel [15] and carbon-dot-Cu<sup>2+</sup> nanoassemblies [16]), conjugating induced photosensitizers-quenching (such as Ce6-Au nanorods [17,18] and Ce6-IR780 [19]) and *etc.* The second step is to turn on the photoactivity by activating sensitizer (B<sub>off</sub>→A<sub>on</sub>) under specific tumor microenvironments (TME), including hypoxia [20], high concentration of glutathione [21], and low pH [22,23]. For instance, fucoidan-based theranostic nanogel is non-phototoxic owing to aggregation-induced self-quenching [15]. After the internalization into cancer cells, the nanogel responds to the intracellular redox potential, namely GSH, thereby enabling the enhanced PDT of tumors. Our group has also developed TME-assisted sensitizers for higher tumor inhibition, including hyaluronidase-induced

\* Corresponding author at: Department of Chemistry, National University of Singapore, 3 Science Drive 3, Singapore 117543, Singapore.

\*\* Corresponding author.

E-mail addresses: [zgchen@dhu.edu.cn](mailto:zgchen@dhu.edu.cn) (Z. Chen), [chmlx@nus.edu.sg](mailto:chmlx@nus.edu.sg) (X. Liu).

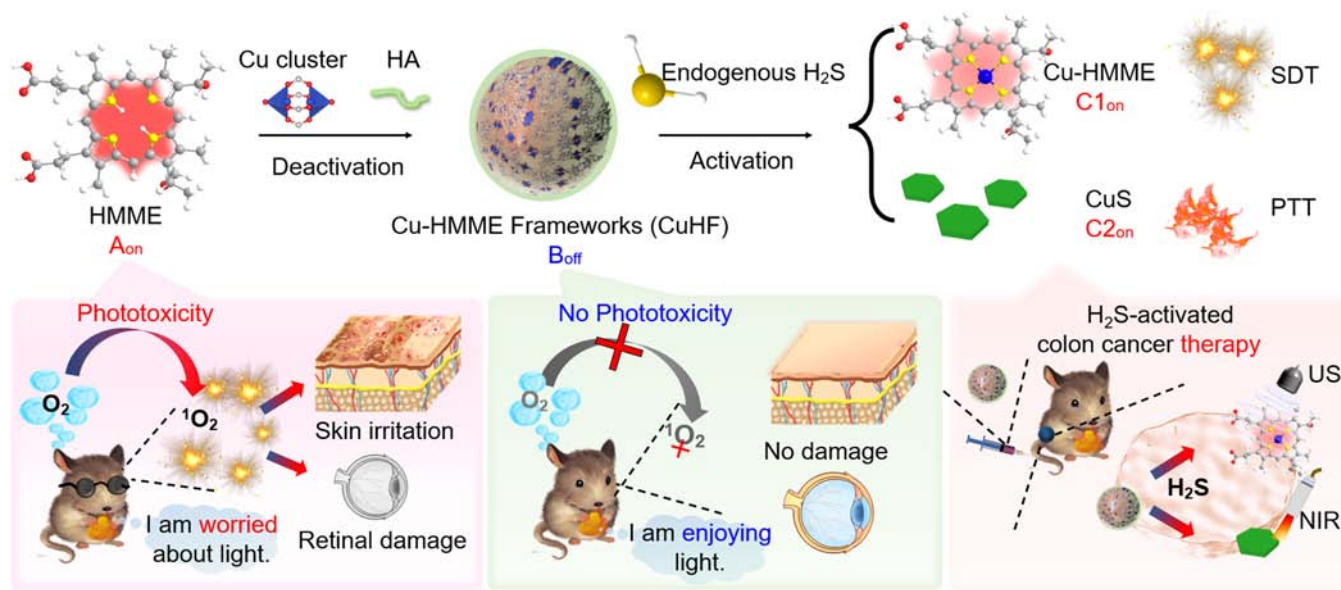
disassembly of hyaluronic acid nanoparticles [24] and GSH-triggered  $\text{Cu}^{2+}$  based chemodynamic effects [25]. It is possible, however, for common tumor microenvironment indicators to overlap with those of other diseases, such as low pH at inflammation and tumor sites, and this may result in undesired activation of the sensitizers [26]. Therefore, it is desirable to exploit ideal sensitizers that are only active in focal zones but are inactive in healthy tissues for the precise therapy.

Hydrogen sulfide ( $\text{H}_2\text{S}$ ), a specific gaseous biomarker in colon cancer, has been identified as an efficient target for activation [27–29]. For examples,  $\text{H}_2\text{S}$  can trigger the conversion (such as  $\text{Cu}_2\text{O} \rightarrow \text{CuS}$  [28],  $\text{Cu}_2\text{O}@\text{CaCO}_3 \rightarrow \text{CuS}$  [30]) of nanoagents for the imaging and/or photothermal therapy. Meanwhile, Cu clusters in frameworks can efficiently harvest charge from organic ligands due to their unsaturated 3d orbitals. Inspired by these features, herein, we reported an on-demand strategy for constructing ideal sensitizers to treat colon tumors, including the deactivation of phototoxicity ( $A_{\text{on}} \rightarrow B_{\text{off}}$ ) of sensitizers and endogenous  $\text{H}_2\text{S}$ -triggered *in-situ* activation ( $B_{\text{off}} \rightarrow C_{\text{on}}$ ) of therapy functions (Scheme 1). As a typical photosensitizer, HMME ( $A_{\text{on}}$ ) can efficiently generate ROS upon light or ultrasound irradiation [31–33]. ROS-induced toxicity cannot discriminate between the cancer cells and normal tissues, causing the damage to vulnerable eyes and skin under sunlight/lamp and thus needing the persistent dodging of light. To alleviate the phototoxicity, HMME was used to coordinate with copper ions ( $\text{Cu}^{2+}$ ) to form Cu-HMME framework (CuHF as  $B_{\text{off}}$ ) nanoparticles (NPs) with sizes of  $\sim 50$  nm, where  $\text{Cu}^{2+}$  coordination could induce a substantial ligand-to- $\text{Cu}^{2+}$  charge-transfer effect [34]. As a result, CuHF NPs exhibited negligible  $^1\text{O}_2$  production, indicating the on-demand deactivation ( $A_{\text{on}} \rightarrow B_{\text{off}}$ ) of phototoxicity. After administration of CuHF, there was no obvious damage to vulnerable skin and retina under simulated sunlight. When CuHF NPs were accumulated in the colon cancer cells, they could react with the endogenous  $\text{H}_2\text{S}$  to induce the *in-situ* conversion ( $B_{\text{off}} \rightarrow C_{\text{on}}$ ), namely on-demand activation, which included the release of Cu-HMME complexes ( $C1_{\text{on}}$ ) for SDT and the formation of CuS nanoparticles ( $C2_{\text{on}}$ ) for photothermal therapy (PTT). After exposure to light and ultrasound, colon cancer cells *in vitro* and *in vivo* were efficiently killed, realizing the precise PTT and SDT against colon cancer.

## Results and discussion

Phototoxicity-free CuHF were first self-assembled using Cu clusters and HMME molecules as building blocks, followed by surface modification with hyaluronic acid. During the synthetic processes,  $\text{Cu}^{2+}$  ions coordinated with the nitrogen in the porphyrin rings of HMME, resulting in the formation of the metalloporphyrin Cu-HMME. The Cu-HMME acted as an organic linker to further coordinate with the secondary building unit  $\text{Cu}_2(\text{CO}_2)_4$ , allowing the assembly of CuHFs with a mean diameter of 50 nm (Fig. 1a, b). CuHF was stable in physiological conditions and dispersed well in phosphate buffered saline (PBS) for 5 days with a low polydispersity index (PDI, 0.19, Fig. S1a, b). The high-resolution transmission electron microscopy (HR-TEM) image showed no lattice fringes, and the fast-fourier transform (FFT, Fig. 1b) pattern had no diffraction spots, indicating that CuHF NPs were amorphous. The homogeneous distribution of Cu/C/N/O in the element mapping also indicated the formation of CuHF NPs (Fig. S2). The zeta potential decreased from  $-14.8$  mV of HMME to  $-5.9$  mV of CuHF (Fig. S3). The bivalent state of Cu elements in the nanoframework was confirmed by X-ray photoelectron spectroscopy (Fig. 1d). In contrast to the 4 Q-band peaks (498, 530, 570 and 622 nm) in the absorption spectrum of HMME, CuHF displayed only two Q-bands at 532 nm and 568 nm, indicating that  $\text{Cu}^{2+}$  occupied the center of the porphyrin (Fig. 1e) [25,35]. Compared with pristine HMME, the fluorescence of CuHF could be quenched over 97% because of the HMME-to- $\text{Cu}^{2+}$  charge transfer (Fig. 1f).

Sensitizers tend to exhibit prolonged photosensitivity, namely phototoxicity that is harmful to skin and vulnerable eyes. To test photoactivity, an aqueous solution of free HMME ( $2 \mu\text{g}/\text{mL}$ ) or CuHF (HMME component:  $2 \mu\text{g}/\text{mL}$ ) was respectively mixed with 1,3-diphenylisobenzofuran (DPBF, a probe), and then irradiated by a 660 nm light for 200 s. The results showed a high DPBF degradation efficiency of 61.5% in HMME group and only 4.6% in the CuHF group (Fig. 2a, S4a, b), indicating that the formation of CuHF efficiently deactivated photosensitivity and  $^1\text{O}_2$  production. The photoactivity was further compared at the cellular level. Unlike HMME which destroyed cells combined with light, CuHF showed little phototoxicity as evidenced by the green fluorescence observed in most



**Scheme 1.** Design of Cu-HMME frameworks (CuHF) for phototoxicity deactivation and synergistic photothermal/sonodynamic therapy (SDT).

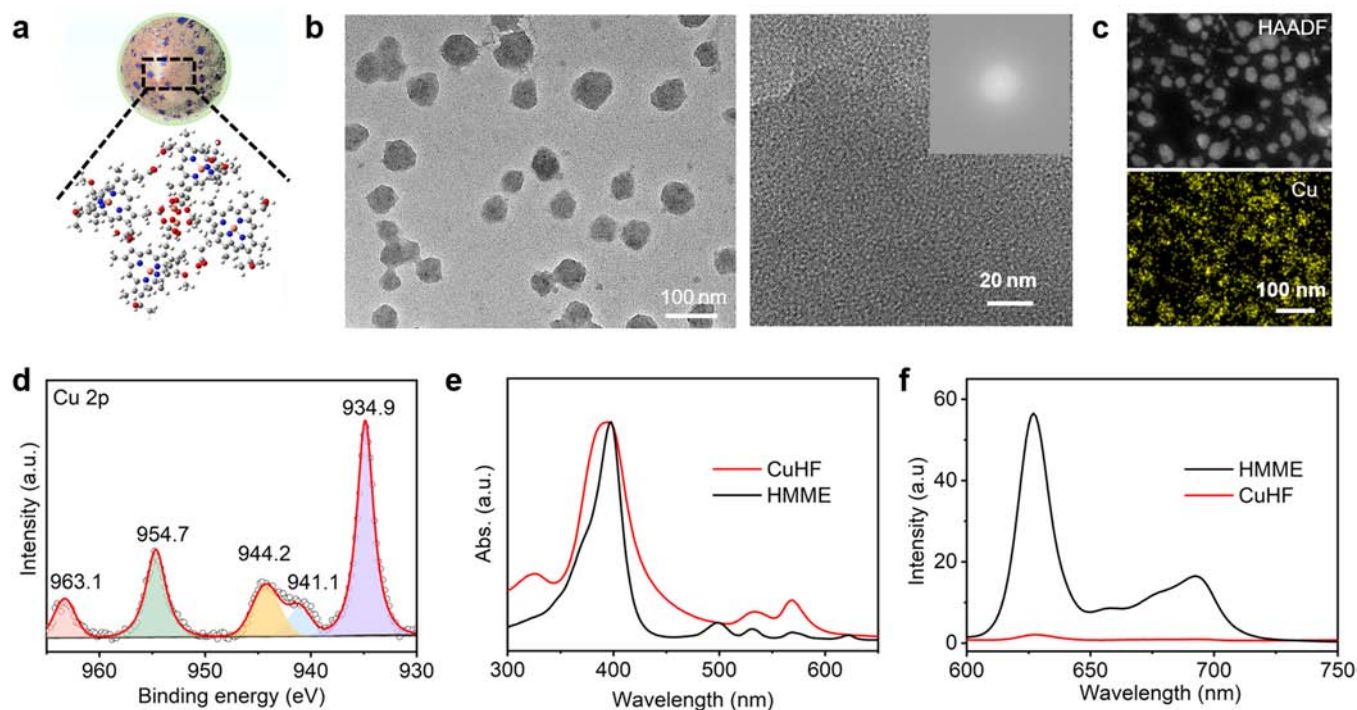


**Fig. 1.** Characterization of CuHF. (a) The proposed unit, (b) transmission electron microscopy image, high-angle annular dark field image, (c) elemental mapping (A high-angle annular dark-field scanning transmission electron microscopy image is abbreviated to HAADF), and (d) high-resolution Cu2p X-ray photoelectron spectroscopy, respectively, of CuHF. (e) UV-vis absorption and (f) photoluminescent spectra (ex, 400 nm) of HMME and CuHF, respectively.

cells (Fig. 2b). Then mice were injected with HMME and CuHF to evaluate phototoxicity to skin and eye (Fig. 2c). After two days, the skin exhibited erythematous swelling, whereas the CuHF-treated area showed no obvious changes (Fig. 2d). Histological analysis of the skin biopsy showed that HMME caused damage to epidermis and vessels (Fig. 2e). This vascular damage due to loss of endothelial cells and formation of microthrombi may result in lymphocytic infiltration and epidermal thickening [36]. However, the skin area of the CuHF-treated group showed clearly distinguishable layers of epidermis and dermis without inflammation or endothelial injury. Apart from the skin lesion, the damage caused by HMME to eyes was much more severe. HMME treatment induced structural disruption and damage to retinal layers in the eyes (Fig. 2f-h). Such uneven thickness of the inner nuclear layer (INL) and outer nuclear layer (ONL) may lead to impaired vision or even blindness [37,38]. Retinal layers remained flat after CuHF treatment, indicating negligible retinal injury.

H<sub>2</sub>S may react with CuHF to release Cu-HMME complexes and generate CuS nanoparticles because of the intrinsic high affinity between Cu and S elements [27,28,39]. One can deduce that the relatively high concentration of endogenous H<sub>2</sub>S in colon cancer may react with CuHF to release Cu-HMME complexes and generate CuS, resulting in the on-demand activation.

By using NaHS to simulate endogenous H<sub>2</sub>S, the release of Cu-HMME complexes was investigated during the vulcanization reaction. The original CuHF solution showed red and somewhat cloudy, and it had an absorption peak at 383 nm (Fig. 3a, b). The absorbance of CuHF solution at 383 nm increased with the addition of NaHS as a H<sub>2</sub>S mimic source. The number of Q-band peaks remained at 2 instead of 4, implying the presence of Cu-HMME complexes [40]. The final CuHF+NaHS solution became clear and transparent due to the disassemble of CuHF and the release of Cu-HMME complexes (inset of Fig. 3b). Moreover, the fluorescence intensity at 627 nm increased 11.9-fold after the addition of 30 mM NaHS (Fig. 3c, d). Cu-HMME complexes were likely to be responsible for the fluorescence, which

was similar to other Cu-based metalloporphyrins, such as Cu (II)TMPyP and CuTUP [40,41]. The release of Cu-HMME complexes would affect the ability of <sup>1</sup>O<sub>2</sub> production under ultrasound irradiation. The <sup>1</sup>O<sub>2</sub> generation of this sulfurized CuHF was 8.3-fold higher than that of the pristine CuHF (Fig. 3e, f and S5a). In addition, the Cu-HMME complexes could not generate <sup>1</sup>O<sub>2</sub> under the excitation of near-infrared region (NIR) light irradiation (Fig. S5b). Therefore, the addition of NaHS released the Cu-HMME complexes and then unlocked the generation ability of <sup>1</sup>O<sub>2</sub>, resulting in the activation of SDT function.

In order to gain insight into the electronic structure, the spin density distributions of HMME, CuHF, and Cu-HMME were simulated based on density functional theory (DFT) calculations (Fig. 3g, S6). Unlike the homogeneous electron distribution of HMME, the highest occupied molecular orbital (HOMO) of CuHF significantly overlapped with the Cu<sub>2</sub>(CO<sub>2</sub>)<sub>4</sub>, while the lowest unoccupied molecular orbital (LUMO) was mainly on metalloporphyrin, showing a higher negative potential on Cu<sub>2</sub>(CO<sub>2</sub>)<sub>4</sub> moiety [42,43]. Meanwhile, the orbital energy level of Cu<sup>2+</sup> (0.62 eV) was lower than the triplet state of Cu-HMME (1.02 eV) and <sup>3</sup>O<sub>2</sub> (0.98 eV[44]). The excitation of the Cu-HMME macrocycle is transferred to the Cu<sub>2</sub>(CO<sub>2</sub>)<sub>4</sub> moiety rather than oxygen. As for Cu-HMME, its electrostatic potential map (ESP) was more homogeneous compared to that of CuHF. Based on the above results, we can deduce that HMME is active and can generate abundant <sup>1</sup>O<sub>2</sub> even under sunlight, causing damage to cells. The deactivated CuHF result in low <sup>1</sup>O<sub>2</sub> yield due to electron transfer and aggregation-enhanced non-radiative transition (heat), avoiding phototoxicity. After activation by sulfide source, CuHF can disassemble and release Cu-HMME complexes, unlocking the ability of <sup>1</sup>O<sub>2</sub> production and then realizing the activation of SDT function.

Numerous nanoplates were formed during the vulcanization of CuHF (Fig. 3h). Lattice fringes with an interplanar *d*-spacing of 2.4 Å were associated with (130) of covellite Cu<sub>1.81</sub>S (PDF#41-0959). Cu

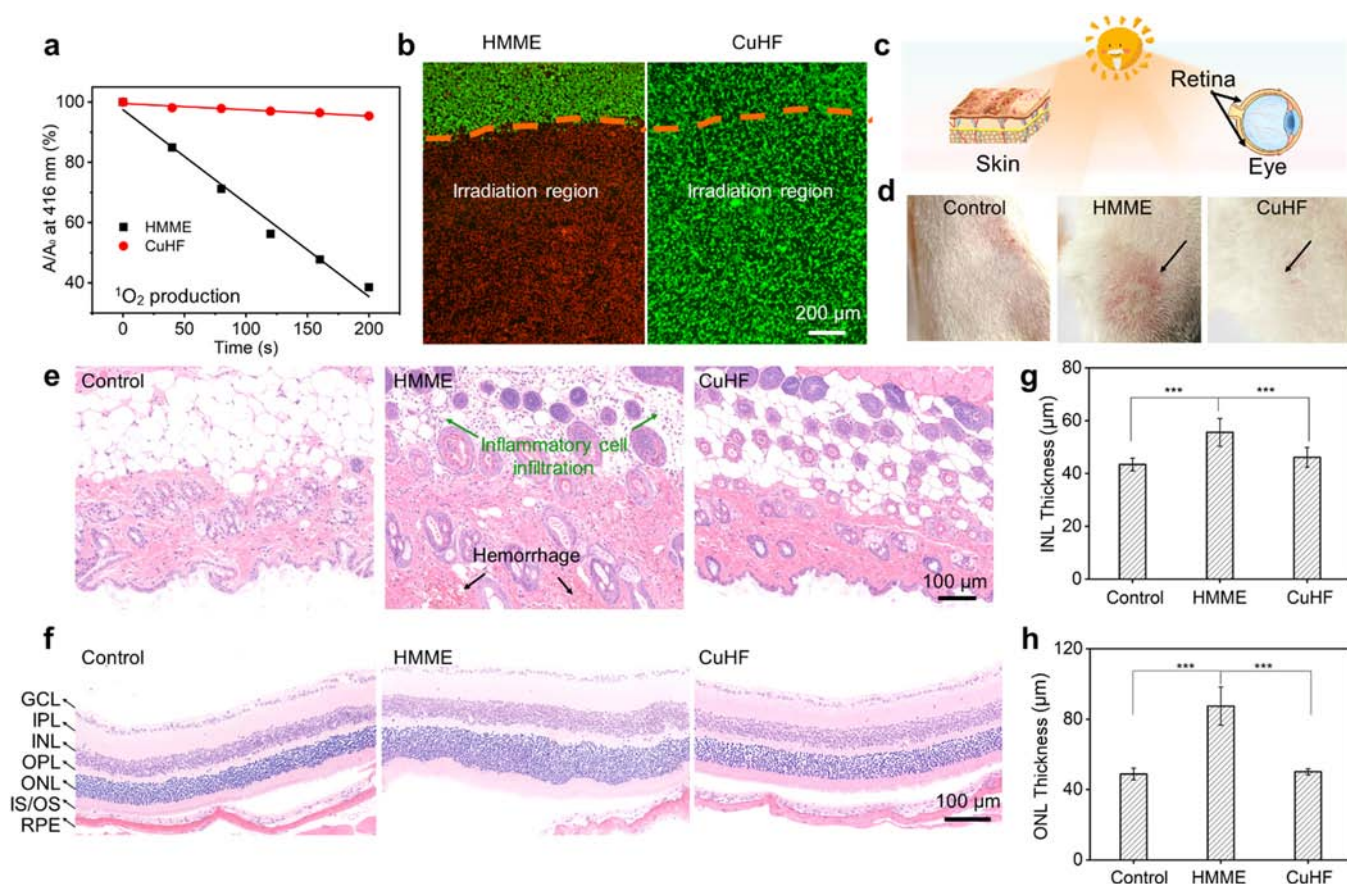


**Fig. 2.** Phototoxicity inhibition of CuHF. (a) Degradation of DPBF by HMME and CuHF. (b) Fluorescence images of cells after treating with HMME or CuHF incubation for 30 min and light irradiations for 10 min (c) Scheme of skin and eye of mice exposed to simulated sunlight. (d) Photographs with the highlighted points of the mice after skin irritation tests. The mice in the control group received no treatment. Hematoxylin and eosin (H&E) stained images of (e) skin and (f) retinal slices after injection with HMME and CuHF, respectively. Quantitative analysis of thickness variation in (g) INL and (h) ONL layers ( $n = 9$ ). Retinal structure in c represents ganglion cell layer (GCL), inner plexiform layer (IPL), inner nuclear layer (INL), outer plexiform layer (OPL), outer nuclear layer (ONL), inner/outer segment (IS/OS), and retinal pigment epithelium (RPE).

and S elements were also homogeneously distributed in the nanocrystals (Fig. S7a, b). The formation of CuS was also confirmed by XPS. The peaks at 932.7 and 952.6 eV in the Cu2p spectrum corresponded to the Cu2p<sub>3/2</sub> and Cu2p<sub>1/2</sub> states of CuS (Fig. S8a), whereas the peaks at 162.4, 163.6, and 168.5 eV in the S2p spectrum represented the S2p<sub>1/2</sub> and S2p<sub>3/2</sub> states of CuS (Fig. S8b) [45]. Additionally, the negligible absorption of pristine CuHF from 700 to 1100 nm increased significantly after the addition of NaHS (Fig. 3i), which could be attributed to the plasma effect of CuS. When irradiated at 808 nm, the temperature of the sulfurized CuHF solution increased 8-fold compared with the pristine solution (Fig. 3j). On-off cycle tests revealed the high photothermal stability and conversion efficiency of the sulfurized solution (Fig. S9a, b). The outstanding photothermal performance of the sulfurized CuHF also led to its multifunctionality in photoacoustic imaging, which would be an added benefit for imaging-guided therapy (Fig. S10). Taken together, NaHS would trigger synergistic anticancer effects of CuHF through sonodynamic and thermal therapeutic modalities.

Further results in the cell counting kit-8 (CCK-8) assays showed negligible cytotoxicity of CuHF with high cell viabilities of over 94.2% (Fig. S11a). The safety of CuHF was also confirmed on normal cells (human umbilical vein endothelial cells, HUVEC) under the ultrasound or NIR irradiation (Fig. S11b). To demonstrate the activation behavior of CuHF *in vitro*, murine colon cancer cells (CT26) were incubated with cystathionine- $\beta$ -synthase (CBS) stimulant sodium butyrate (5 mM) to upregulate H<sub>2</sub>S [27,46]. Red fluorescence appeared and gradually brightened with increasing duration of co-

culture of CuHF and CT26 cells, indicating the release of Cu-HMME complexes (Fig. 4a, b and Fig. S12a, b). The *in vitro* SDT effect of CuHF was evaluated by intracellular ROS quantification (Fig. 4c, Fig. S13). The formation of CuS in CT26 cells through co-incubation with CuHF was characterized by XPS. The high-resolution spectrum of Cu2p showed two peaks at 933.1 eV (Cu2p<sub>3/2</sub>) and 952.8 eV (Cu2p<sub>1/2</sub>) of CuS (Fig. 4d), instead of the four peaks of CuHF. The spectrum of S2p also showed two peaks at 163.7 eV (S2p<sub>1/2</sub>) and 168.6 eV (S2p<sub>3/2</sub>) (Fig. S14). These cellular-level measurements confirmed the chemical transformation of CuHF into Cu-HMME complexes and CuS induced by endogenous H<sub>2</sub>S.

Flow cytometry was performed to quantify cell death induced by photothermal and sonodynamic damage. The results showed that only photothermal treatment caused 69.4% cell death, whereas synergistic therapy yielded a higher ratio of 85.7% (Fig. 4e, f). Therapeutic efficiency was also evaluated by using a dual live/dead cell staining kit (Calcein-AM/PI) and a CCK-8 assay. In the presence of CuHF, red fluorescence increased and cell viability decreased sharply to approximately 50% after NIR irradiation (Fig. 4g and S15a). Moreover, almost all cells died upon simultaneous exposure to ultrasound and NIR irradiation. The combination index (CI) was determined to 0.85 (Fig. S15b), indicating the synergistic therapeutic effect of PTT and SDT (CI < 1) [47]. For cell apoptosis verification, we used the fluorescent probe JC-10 to monitor the mitochondrial membrane potential to reveal the early stage of cell apoptosis. CT26 cells in the I-II and CuHF groups showed strong red fluorescence (Fig. 4h, S16), indicating that JC-10 was aggregated in the

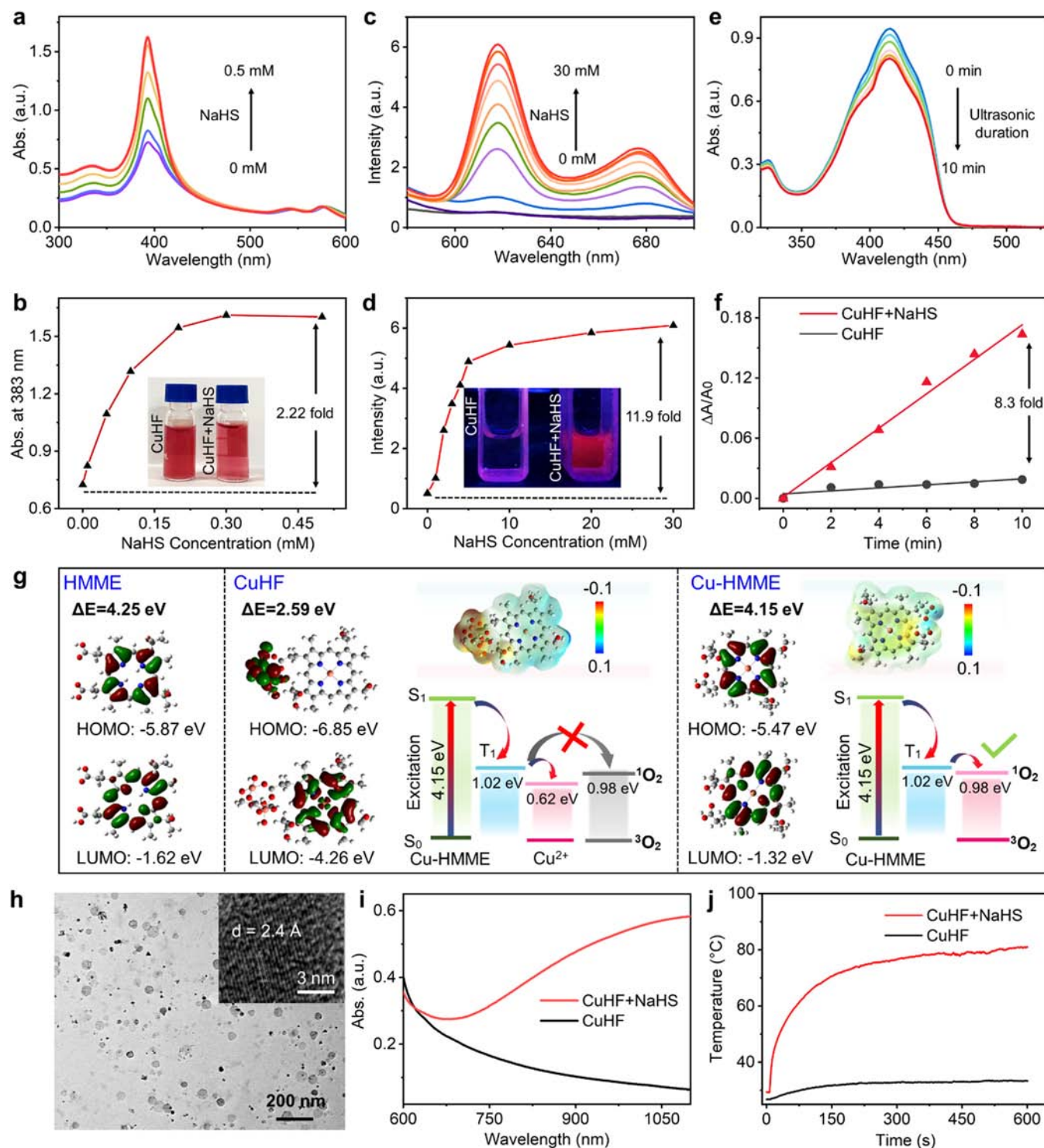


**Fig. 3.** Variation in (a,b) absorption and (c,d) fluorescence before and after addition of NaHS. The inset in b and d ( $\lambda_{\text{ex}}=365 \text{ nm}$ ) is the corresponding photo of the samples. (e,f) DPBF degradation by CuHF and sulfurized CuHF, respectively, under ultrasonic irradiation. (g) Molecular orbital diagram and electrostatic potential (ESP) maps for HMME, CuHF, and Cu-HME. The dramatic decrease in the frontier orbital energy gap of CuHF is due to the significant change in the localization of the highest occupied molecular orbital (HOMO) and the lowest unoccupied molecular orbital (LUMO). (h) TEM image of *in-situ* derived CuS nanoparticles (inset: high-magnification image). (i) UV-vis spectra and (j) time-dependent temperature profiles, respectively, of CuHF with and without NaHS treatment.

mitochondrial matrix, resulting in a high mitochondrial membrane potential due to the high cell activity. On the contrary, JC-10 monomers emitted green signal within cells after PTT and/or SDT treatments, suggesting apoptosis.

Before administration to mice, the hemolysis tests were performed to evaluate the blood safety of CuHF. The hemolysis ratio was lower than 3% even at  $300 \mu\text{g/mL}$ , indicating the good hemocompatibility of CuHF (Fig. S17). The therapeutic effects of CuHF

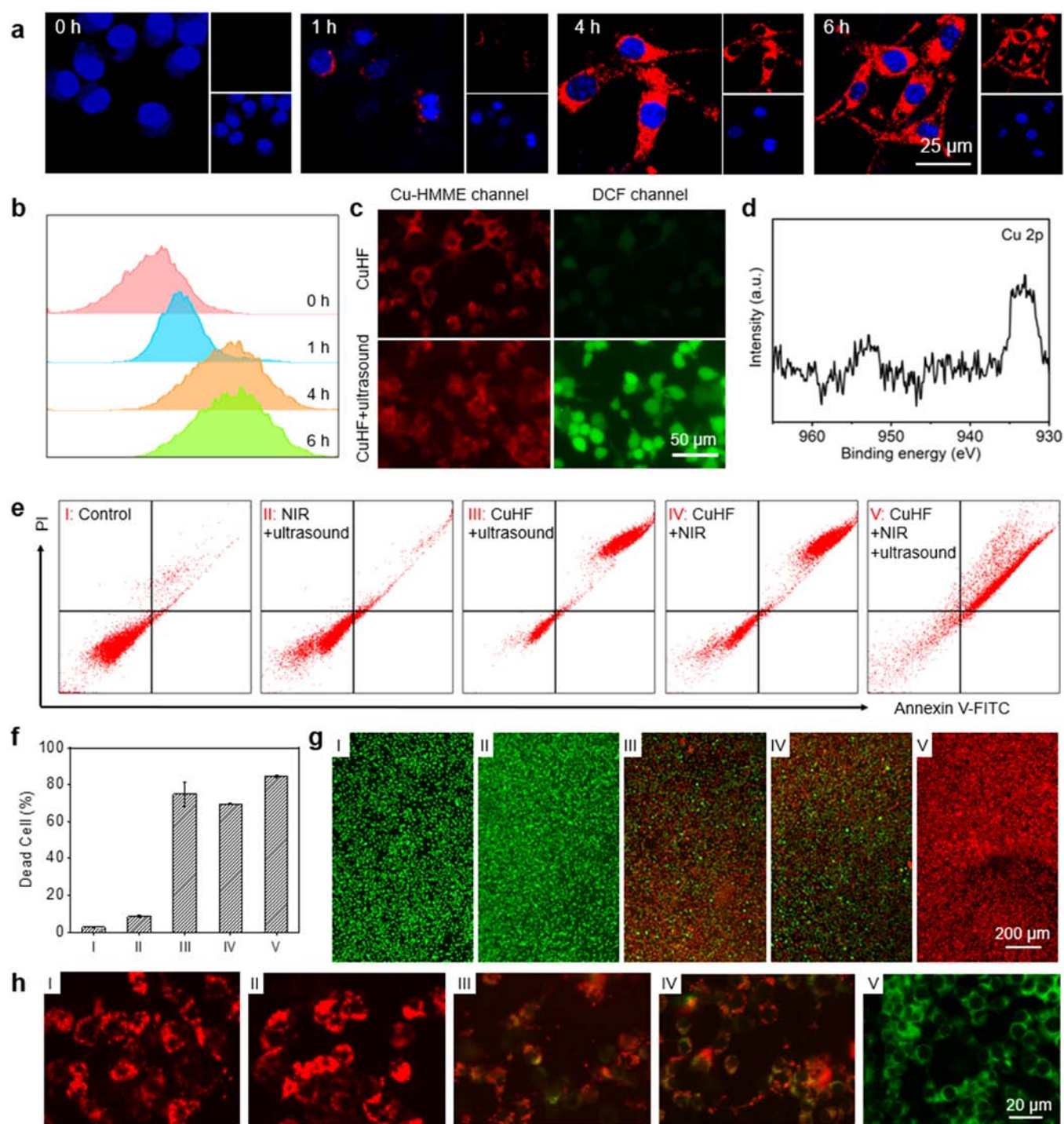


**Fig. 4.** Endogenous H<sub>2</sub>S-triggered activation of CuHF in CT26 cells. (a) Confocal laser scanning microscope images of CT26 cells after incubation with CuHF (DAPI, blue; Cu-HMME, red). (b) Flow cytometric analysis of uptake. (c) Intracellular production of ROS (2',7'-dichlorofluorescein (DCF) channel: green,  $E_x/E_m = 504/529$  nm; Cu-HMME channel: red,  $E_x/E_m = 400/620$  nm). (d) High-resolution XPS Cu 2p and S 2p spectra of cell extracts. (e,f) Flow cytometric analysis and percentage of apoptotic cells from CuHF-cultured cells. (g) Fluorescence images of CT26 stained with calcein AM/PI. (h) The fluorescent images from the JC-10 mitochondrial membrane potential assay after different treatments.

triggered by endogenous H<sub>2</sub>S were further investigated using CT26 tumor models on BALB/c mice (Fig. 5a). As a standard protocol, all mice were injected with S-adenosyl-L-methionine 24 h before experiments to upregulate endogenous H<sub>2</sub>S in tumor [28,48]. After administration of CuHF, their accumulation in the tumor and their conversion to CuS could be visualized due to gradually enhanced

photoacoustic signals (Fig. 5b and Fig. S18). Moreover, tumor temperature increased rapidly in the CuHF-treated group upon NIR irradiation, whereas no obvious changes were detected in the control group (Fig. 5c, d). In addition, the tumor in control groups (PBS or CuHF alone) grew quickly, reaching a 12-fold larger volume after 2 weeks. The tumor growth rate in CuHF-treated groups was

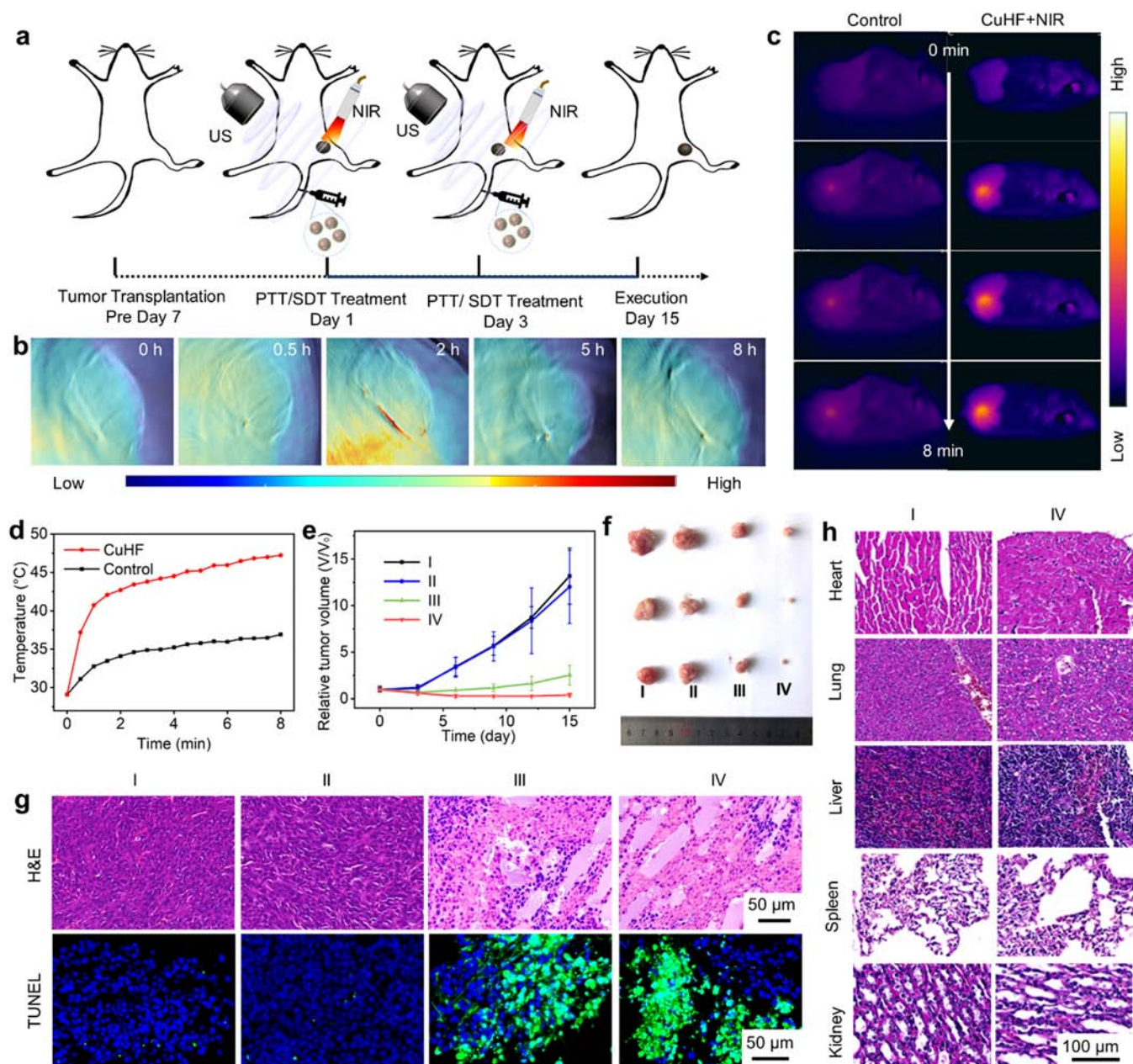


**Fig. 5.** Therapeutic evaluation of CuHF in the colon cancer xenograft model. (a) Flow chart illustrating treatment processes in 15 days. (b) Photoacoustic images at the tumor site after intravenous injection of CuHF at different time points. (c, d) Thermal images and corresponding temperature curves of the mice treated with PBS or CuHF under 808 nm laser irradiation. (e) Variation of tumor volumes at different time points of treatment.  $V_0$  stands for tumor volume before treatments ( $n = 3$ ). (f, g) Photographs and H&E-stained and TUNEL images of tumors. (h) H&E-stained images of heart, lung, liver, spleen, and kidney. The groups, I: PBS; II: CuHF; III: CuHF +NIR; IV: CuHF+NIR+ultrasound.

effectively suppressed by NIR intervention (Fig. 5e, f and S19). The synergistic therapeutic effect was further confirmed by a post-treatment tissue section analysis, which clearly showed condensed nuclei and damaged tumor cell morphology in the CuHF-treated group (Fig. 5g). H&E staining of major organs and weight monitoring also confirmed the biosafety of the combined therapies (Fig. 5h and S20).

## Conclusions

In this work, we have developed CuHF capable of activation on demand in the presence of  $H_2S$ . CuHF exhibit high quenched fluorescence of over 97% and low photosensitivity in normal tissues,

which reduce safety concerns compared with conventional sensitizers. This nanoframework can respond to endogenous  $H_2S$  to generate Cu-HMME complexes and CuS nanoparticles, which then promote efficacy in colon cancer treatment through combined sonodynamic and photothermal effects. Our work sheds light on the rational design of smart sensitizers for precise cancer therapy.

## Experimental section

### Chemicals

Hydrogen peroxide ( $H_2O_2$ ), copper chloride dihydrate ( $CuCl_2 \cdot 2H_2O$ ), 1,3-diphenyl isobenzofuran (DPBF), trimethylamine,

and *N,N*-dimethylformamide (DMF) were brought from Sinopharm Chemical Reagent Co., Ltd. Hematoporphyrin monomethyl ether (HMME) was purchased from Shanghai Xianhui Pharmaceutical Co. Hyaluronic acid (MW: 200 kDa) was purchased from Jiangsu haihua biotechnology co. LTD. S-adenosyl-L-methionine (SAM) was purchased from Shanghai Macklin Biochemical Co., Ltd. Phosphate buffered saline (PBS, pH 7.4) and penicillin-streptomycin solution were obtained from Gibco (NY, USA). Calcein acetoxyethyl ester (Calcein AM), propidium iodide (PI), 2',7'-dichlorodihydrofluorescein diacetate (DCFH-DA) were received from Beyotime Biotechnology. Colon cancer cell CT26 were originally purchased from Type Culture Collection of the Chinese Academy of Sciences, Shanghai, China.

### Synthesis of CuHF

CuHF were synthesized through the assembly of HMME with  $\text{Cu}^{2+}$  ions and modification by hyaluronic acid. Briefly, methanol-triethylamine solution (10 mL, volume ratio: 50:1) containing HMME (10 mg) was mixed with methanol-DMF solution (10 mL, volume ratio: 85:15) containing  $\text{CuCl}_2 \cdot 2\text{H}_2\text{O}$  (10 mg). The mixture was placed in the ultrasonic instrument (40 kHz) and sonicated for 2 h in the dark room. Then, the solution was centrifuged (12000 rpm, 20 min), washed three times with alcohol/water (10 mL, volume ratio: 1:1) and then dispersed in 10 mL of water. Subsequently, hyaluronic acid (20 mg) was added and stirred for overnight. The mixture was centrifuged and washed with deionized water to obtain the final products.

### Physical characterization

TEM imaging and energy dispersive spectroscopy mapping were carried out using a transmission electron microscopy (FEI Talos F200S). XPS was characterized using an Escalab 250Xi instrument. The fluorescence spectra were determined using a fluorescence spectrofluorometer (FP-6600, JASCO). Absorption spectra were measured using a UV-vis spectrofluorometer (Shimadzu UV-3600).

### CuHF activation in solution

NaHS was used to imitate  $\text{H}_2\text{S}$  in solution [30]. The disassembly of CuHF under stimulation of NaHS was confirmed by TEM, UV-vis-NIR, and fluorescence measurements. To confirm the formation of CuS nanoparticles, NaHS (30 mM) was drop into a dispersion of CuHF (0.1 mg/mL) and the mixed solution (CuHF+NaHS) was directly dropwise added onto a copper mesh and dried for TEM measurement. DPBF was employed to detect the generation of  $^1\text{O}_2$ . DMF (2 mL) containing DPBF (20  $\mu\text{L}$ , 2 mg/mL) was mixed with CuHF (2.5  $\mu\text{g}/\text{mL}$ ), followed by irradiation with ultrasound (1.0 MHz, 2.5  $\text{W}/\text{cm}^2$ ) for different periods (0–10 min) in the dark.

### Evaluation of the photothermal effect

A thermal infrared imager was employed to estimate photothermal performance. Firstly, NaHS (0–30 mM) was added into a dispersion of CuHF (0–1 mg/mL) and reacted overnight. The mixed solution was irradiated upon 808 nm excitation (1.5  $\text{W}/\text{cm}^2$ ) for 600 s. Finally, photothermal conversion efficiency ( $\eta_T$ ) was calculated according to the following equation:

$$\eta_T = \frac{hA(\Delta T_{\text{max,dis}} - \Delta T_{\text{max,H}_2\text{O}})}{I(1 - 10^{-A_{808}})}$$

where  $h$  is the heat transfer coefficient,  $A$  is the surface area of the container,  $\Delta T_{\text{max,dis}}$  and  $\Delta T_{\text{max,H}_2\text{O}}$  denote the temperature change at the maximum equilibrium temperature.  $I$  represents the laser power in units of W and  $A_{808}$  is the absorbance at 808 nm.

### Cellular work

CT26 cells were cultured in DMEM medium containing 10% fetal bovine serum and 1% penicillin-streptomycin in the presence of 5%  $\text{CO}_2$  at 37 °C. CT26 cells were planted in a 96-well plate and cultured for 24 h. CuHF (0–100  $\mu\text{g}/\text{mL}$ ) solutions were introduced to the culture medium and co-cultured for another 24 h. To evaluate the safety of CuHF on normal cells, HUVEC were also seeded in a plate and cultured with CuHF (100  $\mu\text{g}/\text{mL}$ ) for 24 h, followed by ultrasound or NIR irradiation. After washing the cells twice with PBS, 100  $\mu\text{L}$  of the CCK-8 were added into the treated cells. After another culture of 4 h, the absorbance at 450 nm was recorded using a microplate reader. Cell viability was calculated as follows: viability (%) =  $100 \times \frac{\text{Abs}_{\text{sample}} - \text{Abs}_{\text{blank}}}{\text{Abs}_{\text{control}} - \text{Abs}_{\text{blank}}}$ .

Cellular uptake of CuHF was measured using a confocal laser scanning microscope (DAPI channel:  $E_x/E_m = 340/488$  nm; Cu-HMME channel:  $E_x/E_m = 400/620$  nm). Briefly, CT26 cells were cultured in dishes containing CuHF and sodium butyrate (5 mM) that can up-regulate CBS expression and  $\text{H}_2\text{S}$  production [27,46,49]. For intracellular ROS detection, the 2',7'-dichlorofluorescein diacetate (DCFH-DA) probe was added to the cultured cells and the fluorescence images were captured (DCF channel: green,  $E_x/E_m = 504/529$  nm; Cu-HMME channel: red,  $E_x/E_m = 400/620$  nm). To validate the therapeutic effect of CuHF, three treatment groups were designed: Group 1, PBS; Group 2, CuHF+NIR; Group 3, CuHF+NIR+ultrasound. The irradiation parameters, ultrasound: 1.0 MHz, 2.5  $\text{W}/\text{cm}^2$ , NIR: 1.5  $\text{W}/\text{cm}^2$ . Cell apoptosis was assessed using flow cytometry and JC-10 staining. To mitigate the impact of red fluorescence from Cu-HMME complexes, a compensation sample containing cells treated only with CuHF was used.

### In vivo work

BALB/c mice (6–8 weeks of age) were obtained from Shanghai SLAC Laboratory Animal Center. All animal works followed the guide for the Care and Use of Laboratory Animals and performed in accordance with protocols approved by the Animal Welfare and Research Ethics Committee of Donghua University.

For skin injury tests, HMME or CuHF (120  $\mu\text{L}$ , 2 mg/mL equivalent HMME) was subcutaneously injected into the healthy mice. The skin was irradiated with stimulated light (0.1  $\text{W}/\text{cm}^2$ ) for 20 min. After 2 days, the skin at the injection site was harvested and sliced for H&E staining. For eye injury tests, HMME or CuHF (120  $\mu\text{L}$ , 2 mg/mL of equivalent HMME) was intravenously injected into the healthy mice. After 1 h of injection, eyes were irradiated with simulated light for 20 min and sliced for H&E staining.

To establish the tumor model in the subcutaneous tissue, CT26 cells ( $1 \times 10^6$  cells) suspended in 100  $\mu\text{L}$  PBS were subcutaneously injected into the right abdomen of each mouse. When the tumor volume reached 50–80  $\text{mm}^3$ , tumor-bearing mice were used for imaging experiments. Before therapeutic experiments, tumor-bearing mice was intraperitoneally injected with an allosteric CBS activator SAM (20 mg/kg) to upgrade the  $\text{H}_2\text{S}$  level [28]. Then, CT26-bearing mice were injected intratumorally or intravenously with a CuHF dispersion (120  $\mu\text{L}$ , 2 mg/mL). Photoacoustic (PA) images of tumor sites were acquired at different time points after injection. To evaluate the effect of therapy *in vivo*, mice were randomly divided into four groups: (I) PBS; (II) CuHF; (III) CuHF+NIR; (IV) CuHF+NIR

+ultrasound. The mice in each group were intravenously injected with 120  $\mu$ L PBS or CuHF (120  $\mu$ L, 13 mg/kg). Then the mice were executed with ultrasound irradiation (1.0 MHz, 2.5 W/cm<sup>2</sup>, 12 min, 25% duty cycle) or 808 nm NIR irradiation (1.0 W/cm<sup>2</sup>, 10 min). Treatments were repeated twice on the first day and on the third day. After 15 days, the tumors, heart, liver, spleen, lungs, and kidneys were collected for histopathological analysis, including H&E staining and terminal deoxynucleotidyl transferase dUTP nick-end labeling (TUNEL) assay.

#### Computational details

To gain insight into the electronic structure, we established a CuHF model of Cu-HMME linked to Cu<sub>2</sub>(CO<sub>2</sub>)<sub>4</sub> and performed calculations based on density functional theory (DFT) [25,50,51]. Optimized molecular geometries were calculated at the BHandHLYP/Def2SVP levels of theory. All calculations were performed using the Gaussian 16 program.

#### Statistical analysis

All data are shown as mean  $\pm$  SD, unless otherwise stated. The significance of differences was determined by analysis of variance (\*  $p < 0.05$ , \*\*\*  $p < 0.001$ ).

#### CRedit authorship contribution statement

**Mei Wen:** Methodology, Investigation, Data curation, Writing – original draft. **Nuo Yu:** Investigation, Methodology. **Zhigao Yi:** Writing – original draft. **Pu Qiu:** Investigation. **Cheng Tao:** Methodology. **Daniel K. Macharia:** Writing – review & editing. **Meifang Zhu:** Funding acquisition. **Zhigang Chen:** Conceptualization, Writing – review & editing, Funding acquisition. **Xiaogang Liu:** Conceptualization, Writing – review & editing.

#### Data Availability

No data was used for the research described in the article.

#### Declaration of Competing Interest

The authors declare that they have no known competing financial interests or personal relationships that could have appeared to influence the work reported in this paper.

#### Acknowledgments

This work was financially supported by the National Natural Science Foundation of China (51972056, 52002061, 52161145406), Program of Shanghai Academic/Technology Research Leader (20XD1420200), Major Science and Technology Innovation Project of Shandong Province (2019JZZY011108), Graduate Student Innovation Fund of Donghua University (CUSF-DH-D-2021010), the National Research Foundation, Prime Minister's Office, Singapore, under the NRF Investigatorship Programme (Award No. NRF-NRFI05-2019-0003), and NUS NANONASH Programme (NUHSRO/2020/002/NanoNash/LOA; R143000B43114).

#### Associated content

The [Supporting Information](http://pubs.acs.org) is available free of charge at <http://pubs.acs.org>.

[Figs. S1–S20 \(PDF\)](#), combination index assay, and hemolysis assay.

#### Appendix A. Supporting information

Supplementary data associated with this article can be found in the online version at [doi:10.1016/j.nantod.2023.101863](https://doi.org/10.1016/j.nantod.2023.101863).

#### References

- [1] X. Li, J.F. Lovell, J. Yoon, X. Chen, *Nat. Rev. Clin. Oncol.* 17 (2020) 657–674.
- [2] X. Lin, S. Liu, X. Zhang, R. Zhu, S. Chen, X. Chen, J. Song, H. Yang, *Angew. Chem. Int. Ed.* 59 (2020) 1682–1688.
- [3] V.G. Deepagan, D.G. You, W. Um, H. Ko, S. Kwon, K.Y. Choi, G.R. Yi, J.Y. Lee, D.S. Lee, K. Kim, I.C. Kwon, J.H. Park, *Nano Lett.* 16 (2016) 6257–6264.
- [4] X. Zhong, X. Wang, L. Cheng, Ya Tang, G. Zhan, F. Gong, R. Zhang, J. Hu, Z. Liu, X. Yang, *Adv. Funct. Mater.* 30 (2020) 1907954.
- [5] P. Huang, X. Qian, Y. Chen, L. Yu, H. Lin, L. Wang, Y. Zhu, J. Shi, *J. Am. Chem. Soc.* 139 (2017) 1275–1284.
- [6] M. Wen, X. Liu, N. Yu, P. Qiu, D.K. Macharia, M. Li, H. Zhang, Z. Chen, W. Lian, *J. Colloid Interf. Sci.* 626 (2022) 77–88.
- [7] Q. Wang, Y.S. Ji, J.S. Shi, L.L. Wang, *ACS Appl. Mater. Interfaces* 12 (2020) 23677–23688.
- [8] M. Wen, J. Shen, Z. Wang, H. Guo, P. Geng, N. Yu, M. Li, H. Zhang, M. Zhu, Z. Chen, *Nanoscale* 13 (2021) 5910–5920.
- [9] J. Zhou, Z. Hu, F. Zabihi, Z. Chen, M. Zhu, *Adv. Fiber Mater.* 2 (2020) 123–139.
- [10] H.T. Li, X.Y. Song, C. Yang, Q. Li, D. Tang, W.R. Tian, Y. Liu, *Photo Photodyn. Ther.* 10 (2013) 414–421.
- [11] Y. Zhao, P. Tu, G. Zhou, Z. Zhou, X. Lin, H. Yang, Z. Lu, T. Gao, Y. Tu, H. Xie, Q. Zheng, Y. Gu, J. Tao, X. Zhu, *PLoS One* 11 (2016) 156219.
- [12] Z. Wang, L. Huang, Y. Yan, A.M. El-Zohry, A. Toffoletti, J. Zhao, A. Barbon, B. Dick, O.F. Mohammed, G. Han, *Angew. Chem. Int. Ed.* 59 (2020) 16114–16121.
- [13] Z. Huang, *Technol. Cancer Res. Treat.* 4 (2005) 283–293.
- [14] B. Li, X. Wang, L. Chen, Y. Zhou, W. Dang, J. Chang, C. Wu, *Theranostics* 8 (2018) 4086–4096.
- [15] M.H. Cho, Y. Li, P.C. Lo, H. Lee, Y. Choi, *Nanomicro. Lett.* 12 (2020) 47.
- [16] S. Sun, Q. Chen, Z. Tang, C. Liu, Z. Li, A. Wu, H. Lin, *Angew. Chem. Int. Ed.* 59 (2020) 21041–21048.
- [17] J. Wang, M. You, G. Zhu, M.I. Shukoor, Z. Chen, Z. Zhao, M.B. Altman, Q. Yuan, Z. Zhu, Y. Chen, C.Z. Huang, W. Tan, *Small* 9 (2013) 3678–3684.
- [18] J. Wang, G. Zhu, M. You, E. Song, M.I. Shukoor, K. Zhang, M.B. Altman, Y. Chen, Z. Zhu, C.Z. Huang, W. Tan, *ACS Nano* 6 (2012) 5070–5077.
- [19] Y. Zhang, L. He, J. Wu, K. Wang, J. Wang, W. Dai, A. Yuan, J. Wu, Y. Hu, *Biomaterials* 107 (2016) 23–32.
- [20] M. Wang, M.Y. Chang, Q. Chen, D.M. Wang, C.X. Li, Z.Y. Hou, J. Lin, D.Y. Jin, B.G. Xing, *Biomaterials* 252 (2020) 12.
- [21] F. Gong, L. Cheng, N. Yang, O. Betzer, L. Feng, Q. Zhou, Y. Li, R. Chen, R. Popovtzer, Z. Liu, *Adv. Mater.* 31 (2019) 1900730.
- [22] X. Zhao, S. Long, M. Li, J. Cao, Y. Li, L. Guo, W. Sun, J. Du, J. Fan, X. Peng, *J. Am. Chem. Soc.* 142 (2020) 1510–1517.
- [23] M. Borkowska, M. Siek, D.V. Kolygina, Y.I. Sobolev, S. Lach, S. Kumar, Y. Cho, K. Kanderę Grzybowska, A. Bartosz, *Nat. Nanotechnol.* 15 (2020) 331–341.
- [24] M. Wen, N. Yu, S. Wu, M. Huang, P. Qiu, Q. Ren, M. Zhu, Z. Chen, *Bioact. Mater.* 18 (2022) 242.
- [25] N. Yu, P. Qiu, Q. Ren, M. Wen, P. Geng, D.K. Macharia, M. Zhu, Z. Chen, *ACS Nano* 15 (2021) 19793–19805.
- [26] A. Riemann, A. Ihling, J. Thomas, B. Schneider, O. Thews, M. Gekle, *Biochim. Biophys. Acta Biomembr.* 2015 (1853) 299–307.
- [27] Y. Ma, X. Li, A. Li, P. Yang, C. Zhang, B. Tang, *Angew. Chem. Int. Ed.* 56 (2017) 13752–13756.
- [28] L. An, X.D. Wang, X.C. Rui, J.M. Lin, H. Yang, Q.W. Tian, C. Tao, S.P. Yang, *Angew. Chem. Int. Ed.* 57 (2018) 15782–15786.
- [29] C. Szabo, C. Coletta, C. Chao, K. Modis, B. Szczesny, A. Papapetropoulos, M.R. Hellmich, *Proc. Natl. Acad. Sci. USA* 110 (2013) 12474–12479.
- [30] M. Chang, Z. Hou, D. Jin, J. Zhou, M. Wang, M. Wang, M. Shu, B. Ding, C. Li, J. Lin, *Adv. Mater.* 32 (2020) 2004647.
- [31] K.H. Yuan, Z. Huang, *Photo Photodyn. Ther.* 4 (2007) 149–150.
- [32] J.K. Chen, P. Ghasri, G. Aguilar, A.M. van Drooge, A. Wolkerstorfer, K.M. Kelly, M. Heger, *J. Am. Acad. Dermatol.* 67 (2012) 289–304.
- [33] P. Sun, X. Zhao, Y. Zhou, Y. Liang, H. Zhang, Y. Cui, J. Tao, *Acta Pharmacol. Sin.* 32 (2011) 1549–1554.
- [34] Y.T. Li, J.L. Zhou, L. Wang, Z.G. Xie, *ACS Appl. Mater. Interfaces* 12 (2020) 30213–30220.
- [35] P. Huang, X. Qian, Y. Chen, L. Yu, H. Lin, L. Wang, Y. Zhu, J. Shi, *J. Am. Chem. Soc.* 139 (2017) 1275–1284.
- [36] J. Li, N. Kirkiles-Smith, J. McNiff, J. Pober, *J. Immunol.* 171 (2003) 1526–1533.
- [37] J.J. Dunmire, R. Bouhenni, M.L. Hart, B.T. Wakim, A.M. Chomyk, S.E. Scott, H. Nakamura, D.P. Edward, *Mol. Vis.* 17 (2011) 779–791.
- [38] K. Wang, M. Zheng, K.L. Lester, Z. Han, *Sci. Rep.* 9 (2019) 14573.
- [39] M. Ma, Y. Yao, Y. Wu, Y. Yu, *Adv. Fiber Mater.* 2 (2020) 314–337.

- [40] J. Li, Y. Wei, L. Guo, C. Zhang, Y. Jiao, S. Shuang, C. Dong, *Talanta* 76 (2008) 34–39.
- [41] M. Bahrami, S. Kraft, J. Becker, H. Hartmann, B. Vogler, K. Wardelmann, H. Behle, J.A.A.W. Elemans, I. Barke, S. Speller, *J. Phys. B. Mol. Opt.* 51 (2018) 144002.
- [42] N. Ikuma, S. Inaba, K. Kokubo, T. Oshima, *Chem. Comm.* 50 (2014) 581–583.
- [43] Z. Aliakbar Tehrani, Z. Jamshidi, H. Farhangian, *J. Mol. Model.* 19 (2013) 4763–4772.
- [44] K. Wen, H. Tan, Q. Peng, H. Chen, H. Ma, L. Wang, A. Peng, Q. Shi, X. Cai, H. Huang, *Adv. Mater.* 34 (2022) 2108146.
- [45] R.M.Y. Saeed, Z. Bano, J.Z. Sun, F.Y. Wang, N. Ullah, Q.Q. Wang, *J. Appl. Polym. Sci.* 136 (2019) 10.
- [46] Q. Cao, L. Zhang, G. Yang, C. Xu, R. Wang, *Antioxid. Redox Signal.* 12 (2010) 1101–1109.
- [47] Y. Zhao, M. Wen, N. Yu, C. Tao, Q. Ren, P. Qiu, Y. Zhang, Y. Wang, J. Xia, Z. Chen, *J. Colloid Interf. Sci.* 637 (2023) 225–236.
- [48] K. Módis, C. Coletta, A. Asimakopoulou, B. Szczesny, C. Chao, A. Papapetropoulos, M.R. Hellmich, C. Szabo, *Nitric Oxide* 41 (2014) 146–156.
- [49] S. Mimoun, M. Andriamihaja, C. Chaumontet, C. Atanasiu, R. Benamouzig, J.M. Blouin, D. Tome, F. Bouillaud, F. Blachier, *Antioxid. Redox Signal.* 17 (2012) 1–10.
- [50] S.S.Y. Chui, S.M.F. Lo, J.P.H. Charmant, A.G. Orpen, I.D. Williams, *Science* 283 (1999) 1148–1150.
- [51] G. Aquilanti, M. Giorgetti, M. Minicucci, G. Papini, M. Pellei, M. Tegoni, A. Trasatti, C. Santini, *Dalton Trans.* 40 (2011) 2764–2777.